Massachusetts Institute of Technology

Multi-Fidelity High-Throughput Optimization of Electrical Conductivity in P3HT-CNT Composites

Daniil Bash, Yongqiang Cai, Vijila Chellappan, Swee Liang Wong, Xu Yang, Pawan Kumar, Jin Da Tan, Anas Abutaha, Jayce JW Cheng, Yee-Fun Lim, Siyu Isaac Parker Tian, Zekun Ren, Flore Mekki-Berrada, Wai Kuan Wong, Jiaxun Xie, Jatin Kumar, Saif A. Khan, Qianxao Li,* Tonio Buonassisi,* and Kedar Hippalgaonkar*

Combining high-throughput experiments with machine learning accelerates materials and process optimization toward user-specified target properties. In this study, a rapid machine learning-driven automated flow mixing setup with a high-throughput drop-casting system is introduced for thin film preparation, followed by fast characterization of proxy optical and target electrical properties that completes one cycle of learning with 160 unique samples in a single day, a >10× improvement relative to quantified, manual-controlled baseline. Regio-regular poly-3-hexylthiophene is combined with various types of carbon nanotubes, to identify the optimum composition and synthesis conditions to realize electrical conductivities as high as state-of-the-art 1000 S cm^{-1}. The results are subsequently verified and explained using offline high-fidelity experiments. Graph-based model selection strategies with classical regression that optimize among multi-fidelity noisy input-output measurements are introduced. These strategies present a robust machine-learning driven high-throughput experimental scheme that can be effectively applied to understand, optimize, and design new materials and composites.

1. Introduction

One of the biggest bottlenecks for fast and efficient scientific discoveries is the bandwidth and cognitive ability of human researchers, who can conceive, conduct, and comprehend a limited number of experiments. With the emergence of automation, timelines for scientific progress can be significantly accelerated via the implementation of high-throughput experiments. From the first automated pipette in 1950[1] to modern self-driving laboratories,[2–4] automation tools allow researchers to explore complex, multi-dimensional parameter spaces, while freeing up researchers' bandwidth for planning experiments and analyzing data. Datasets generated from computational studies have enabled estimation of electronic,[5] thermal,[6] and thermoelectric[7,8] properties from material compositions and structures, and augmented by machine learning models. With, machine learning employed as a cognitive assistant to plan and navigate complex parameter spaces, a new paradigm has emerged in recent years which is particularly useful for combinatorial experiments[9–13] and multi-variable optimization problems.[14–16] These methods have been used for discovery of novel metal alloys,[13,14,17–19] perovskite materials for photovoltaics,[2,15,20] electronic property optimization of polymer thin films,[2,3] or synthesis of co-polymers with pre-defined target properties.[21]

Machine Learning (ML) assisted materials property optimization is particularly useful in solution processable organic-inorganic hybrid materials because the final material property or device performance of this class of materials is highly

D. Bash, Dr. V. Chellappan, Dr. S. L. Wong, Dr. X. Yang, Dr. P. Kumar, J. D. Tan, Dr. A. Abutaha, Dr. J. J. Cheng, Dr. Y.-F. Lim, Dr. J. Kumar, Prof. K. Hippalgaonkar
Institute of Materials Research and Engineering (IMRE)
Agency for Science
Technology and Research (A*STAR)
#08-03, 2 Fusionopolis Way, Innovis, Singapore 138634, Singapore
D. Bash, Dr. Y. Cai, J. D. Tan, S. I. P. Tian, Z. Ren, Dr. F. Mekki-Berrada, W. K. Wong, J. Xie, Prof. S. A. Khan, Prof. Q. Li
National University of Singapore
3 Science Drive 3, Singapore 117543, Singapore
E-mail: qianxiao@nus.edu.sg

The ORCID identification number(s) for the author(s) of this article can be found under https://doi.org/10.1002/adfm.202102606.

DOI: 10.1002/adfm.202102606

S. I. P. Tian, Z. Ren, Prof. T. Buonassisi
Singapore-MIT Alliance for Research and Technology
1 Create Way, #10-01 & #09-03 CREATE Tower, Singapore
138602, Singapore
E-mail: buonassisi@mit.edu
Prof. Q. Li
Institute of High-Performance Computing (IHPC)
Agency for Science
Technology and Research (A*STAR)
1 Fusionopolis Way, #16-16 Connexis, Singapore 138632, Singapore
Prof. K. Hippalgaonkar
Nanyang Technological University
50 Nanyang Ave, #01-30 General Office, Block N4.1, Singapore
639798, Singapore
E-mail: kedar@ntu.edu.sg

**ADVANCED
SCIENCE NEWS**

www.advancedsciencenews.com

**ADVANCED
FUNCTIONAL
MATERIALS**

www.afm-journal.de

influenced by multiple factors such as chemical structure, purity, processing solvents, solvent additives, nano-phase separation, and interface/device engineering. Screening of suitable molecular structures, with process parameters determined by ML techniques has enabled rapid development of optoelectronic devices such as organic photovoltaics.[22] ML algorithms can effectively learn from the vast amount of data on chemical/electronic structures and build suitable models to predict the underlying material characteristics with reasonable accuracy, accelerating the discovery of high-performance materials. Yao et al. used random forest (RF) and boosted regression trees (BRT) to screen >32 millions of donor/acceptor pairs to identify six pairs of efficient organic photovoltaic material combinations for experimental validation.[23] The benefits of using ML methods to predict macroscopic device properties from microscopic structures are highlighted by Florian Häse et al.[24] Wu et al. have successfully synthesized a high performance thermoelectric polymeric material using machine learning assisted polymer chemistry.[25]

In this report, we present a high-throughput semi-automated experimental platform driven by machine learning to maximize the electrical conductivity of inorganic-organic hybrid materials. As an integral part of this platform, Bayesian optimization is performed for targeted sampling of data, which is then used to build and select robust Graphical-based Models that link multiple experimental inputs to outputs. These can then be used for analysis and design of high-performance materials for desired applications, as machine learning is exceptionally powerful in multi-parameter optimization, in contrast to traditional design of experiments where only one variable is tuned at a time.

We chose solution processable semiconducting polymer/nanotube composites as a materials system of choice because they combine the advantages of mechanical flexibility and low-cost manufacturing processes, making them suitable for electronic and thermoelectric applications. In particular, we chose regio-regular poly-3-hexylthiophene (rr-P3HT) as a polymer matrix, as it is a well-studied and understood system, and it still has potential for improvement as the polymer matrix in thermoelectric composites, as shown by Pawan Kumar et al.,[26] in contrast to other well-studied semiconducting polymers.

We used our machine learning driven high-throughput experimental platform to demonstrate optimization of electrical conductivity in rr-P3HT and carbon nanotube (CNT) composites. Such composite films of conjugated polymers with single-, double- or multiwall carbon nanotubes (SWCNTs, DWCNTs, or MWCNTs) have been used as an active material in various functional devices due to their unique optical, electrical and mechanical properties.[27–30] However, the electrical conductivity (σ) of P3HT/CNT composites requires significant improvement in order to make this class of nanocomposites viable for practical applications. Various strategies are proposed to increase the electrical conductivity of P3HT/CNT composites including molecular doping of P3HT, use of different CNT types,[31] process optimization, tuning the energy barrier between the polymer and CNT[32] and improvement of the crystalline structure or morphology of P3HT and CNT.[33–35] Most of these approaches are concentrated on enhancing inter-chain charge transport by improving the degree of crystallinity or nanoscale

architecture of P3HT chains induced by CNTs.[36] The configuration of P3HT wrapping around the CNTs, particularly the formation of elongated polymer chain conformation with reduced torsional disorder, promotes inter-chain (π–π stacking) interaction and thus increases charge mobility.[28] However, the degree of crystallinity and orientation of π–π stacking depends on the interaction between P3HT and CNT where parameters such as type, size, and length of CNTs manipulates the crystalline packing structure, thus influencing the charge transport.[28,31] In addition to CNT-induced charge carrier mobility enhancement, chemical doping of P3HT increases the electrical conductivity since doping of conjugated polymers with small molecular oxidizers such as 2,3,5,6-tetrafluoro-7,7,8,8-tetracyanoquinodimethane (F4-TCNQ) or iron(III) chloride ($FeCl_3$) introduces mobile charges to the conjugated polymer chain, which increases charge carrier concentration and reduces π–π stacking distances due to structural reorganization and polaron delocalization.[37–39] Therefore, there is a rich interaction space available where by changing the type of CNTs and tuning the physical and chemical interactions can potentially enhance the electrical conductivity.

In this study, we mix rr-P3HT with four types of CNTs, where the interactions between the P3HT chains and CNTs are expected to create different morphologies and crystalline structures that control the electrical conductivity of the composite film. The types of CNTs used in this study are: 1) long single wall CNTs of lengths in the range of 5–30 µm (l-SWNTs), 2) short single wall CNTs of lengths in the range of 1–3µm, (s-SWNTs), 3) multi walled CNTs (MWCNTs), and 4) double-walled CNTs (DWCNTs). The choice of the nanotubes was aimed to cover a broad range of properties, by focusing on most widely used range of the nanotube types. Broader parameter space of nanotube properties (such as geometry and chirality control, metallicity etc.) could in theory be studied, however we felt it more appropriate to study the space of nanotube attributes most widely used by the scientific community first. Further details of the materials can be found in Section S1.1, Supporting Information. All the composite films are doped with $FeCl_3$ in order to increase the overall electrical conductivity. It has already been reported that doping increases the electrical conductivity of all P3HT/CNT composites irrespective of the type of CNTs.[31] The workflow begins with data generation from the high-throughput experimental platform, where P3HT/CNT composite films are prepared in a microfluidic reactor linked to an automated drop-casting system, then transitions to rapid optical, and electrical diagnostics, ending the cycle with using obtained data to run a Bayesian Optimization algorithm to scan the experimental manifold and explore input-output correlations to suggest next experimental conditions targeting high conductivity.

2. Data Generation: High Throughput Experiments with Bayesian Optimization

We first apply Bayesian Optimization (BO)[40,41] to optimize the high-throughput processing and characterization, and explore the parameter space for P3HT/CNT composites. This work is based on a hypothesis that a certain combination of CNTs and
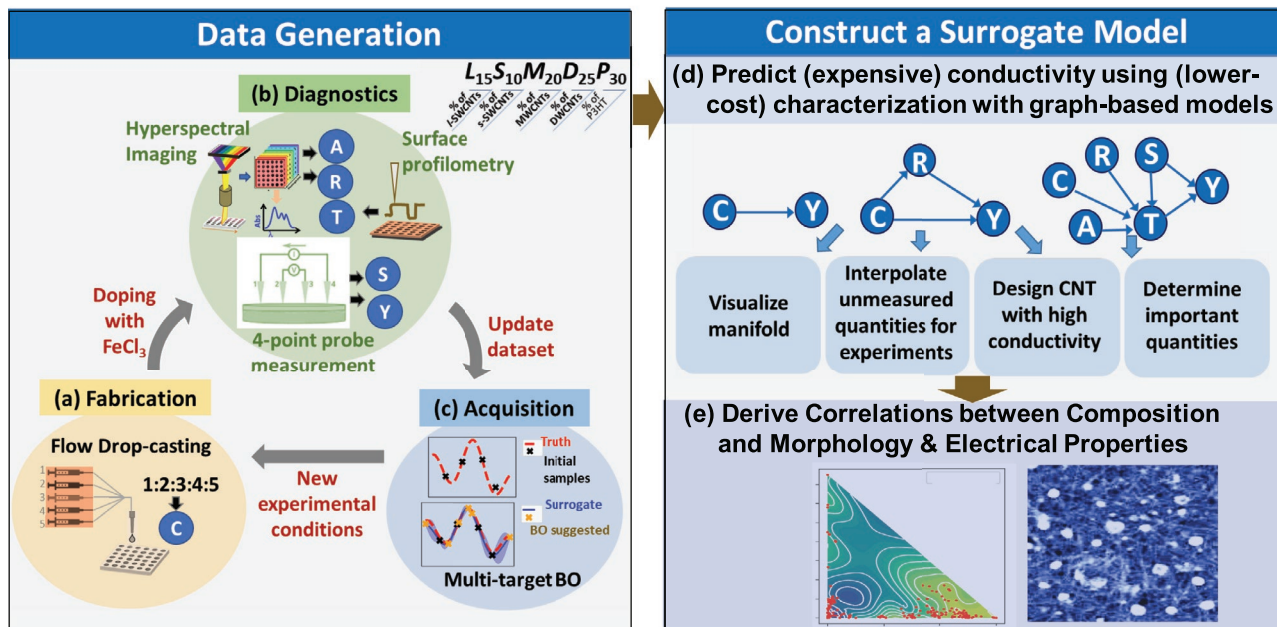
Figure 1. Schematic representation of the workflow involving high-throughput experimental platform for film fabrication and data generation (a–c), and machine learning-based data analysis (d,e). a) Film fabrication. The workflow begins with the preparation of hybrid solution by mixing the pre-prepared P3HT and CNTs stock solutions (1 mg mL^{-1} in o-dichlorobenzene) using an automated microfluidic flow reactor. The microfluidic flow reactor, operated in a plug flow mode, is capable of mixing five different liquids in a precise ratio and separates them as "plugs" containing unique composition ratio (C) of P3HT and CNT. Five liquids include pure P3HT solution, and four CNT dispersions containing different types of CNTs, along with some P3HT as stabilizing surfactant. 36 droplets of P3HT/CNT mixtures are then drop-casted on pre-treated quartz (fused silica) wafer placed on a computer controlled XY stage. These 36 samples contain six unique compositions, where each condition has six replicates in order to check the reproducibility of the films. The drop-casted films are doped with FeCl$_3$ after recording the Hyperspectral image of pristine films. b) Fast optical/electrical diagnostics: Hyperspectral image (spectral region from 400 to 1000 nm) of the drop-casted pristine films (before doping) and doped films are obtained. The absorption spectra of each film are obtained by averaging ≈20 pixels (area of 2.4 sq. mm) in the middle of the droplet. The absorbance ratio (R) between the interchain transition due to π–π stacking (≈602 nm) and intrachain transition due to π–$\pi*$ is recorded as one of the proxy measurements to relate to the electrical conductivity of the film. The absorption spectra of the doped films are also recorded where the absorbance at 525nm (A) is measured for evaluation of the thickness of the doped films. The sheet resistance (S) of the doped films is tested using automated four-point probe measurement and then film thickness (T) of random 15% of the doped films is measured using a surface profilometer. c) Use of Bayesian optimisation (BO) to explore the electrical and optical characteristics related to the input processing/mixing conditions. The surrogate model in BO is a Gaussian process regressor. d) Construction of graphical regression models taking the absorbance, absorbance ratio, and sheet resistance into account to exploit maximal useful information when predicting electrical conductivity. e) The selected graphs are applied to derive correlations between the composition and electrical conductivity for interpretable machine learning.

P3HT should sensitively affect the alignment of P3HT chains to change the conductivity of the system, while dispersed nanotubes, due to their unique dimensionality, would act as seeds for P3HT crystallization. This hypothesis is qualitatively explored via high-throughput experimentation and machine learning. The schematic representation of the entire workflow is shown in **Figure 1** in following steps: a) film fabrication; b) fast optical/electrical labeling; c) use of Bayesian Optimization for targeted exploration of the composition space. Subsequently, once experimental cycles-of-learning are completed, the analysis is done via d) construction of ML models for predicting electrical conductivity through graphical regression models; and e) to derive correlation between the composition and electrical conductivity for interpretable ML. The high-throughput experimental platform consists of a LabView-controlled automatic flow reactor (in plug flow mode), where formulations of different starting materials with varying composition ratios are mixed in situ. The mixing volume and ratio between the stock solutions (details on preparation of stock solutions can

be found in Section S1.2, Supporting Information) are adjusted in order to prepare unique formulations. Each formulation forms a droplet and multiple droplets are subsequently drop-casted onto a pre-cleaned smooth, double-side polished fused silica (quartz) wafer, eliminating the time-consuming process of cleaning and surface treatment of individual substrates. The optical and electrical properties of the drop-casted films are measured using a high-throughput diagnostic platform, which consists of a visible range (400–1000 nm) hyperspectral imaging system and a computer-controlled automated four-point probe setup (Figure 1b). This platform drives the BO algorithm for optimization of the electrical and optical characteristics, that relates them to the input processing/mixing conditions.

2.1. High Throughput Experiments

The hybrid solutions are mixed using a microfluidic flow reactor in order to fully exploit the composition space. The

reactor consists of five computer-controlled syringe pumps, a mixing chamber, a gas-inlet T-junction, and a gas flow controller. This setup allows to mix five different stock solutions together in precise ratios and separate the flow into "plugs" using N_2 gas. The mixed precursor solutions are then drop-casted onto the substrates in an automated high-throughput fashion, via a computer-controlled XY stage, connected to the flow reactor. The samples then undergo post–treatment in the form of doping, to enhance the electrical conductivity of the polymer matrix (refer Section S1.4, Supporting Information for more details).

The drop-casted films before and after doping are screened using hyperspectral imaging (HSI) system that measures the optical absorbance spectra in the visible to near-infrared region (400–1000 nm). The detailed HSI measurement protocols can be found in Section S2.1, Supporting Information. The absorption spectra of P3HT/CNT composite films without post treatment are used to probe the degree of π–π stacking in P3HT. The absorption spectra of P3HT/CNT composite films generally show a peak at 525 nm, which corresponds to the intra-chain (π–π^*) transition and the peaks at 550 and 602 nm correspond to vibronic and interchain transition due to π–π stacking respectively (refer Figures S1 and S2, Supporting Information for more details). The intensity of inter-chain transitions increases when the number of well-ordered P3HT aggregates increases. Therefore, we use absorption ratio (R) (ratio between the inter-chain interaction and intra-chain interaction) as one of the labeled measurements to correlate to the electrical conductivity (σ). The absorption ratio (R) of pristine films along with composition ratio (C) is used to train the ML algorithm to increase the degree of π–π stacking, which is hypothesized to increase the electrical conductivity of the P3HT/CNT composite. The doped films also undergo hyperspectral imaging in order to obtain the absorbance data after doping, where the absorbance (A) at 525 nm is obtained to analyze the effect of CNT loading in the composite. Then the sheet resistances (S) of the doped films are measured using automated 4-point probe system, following which the films undergo surface profilometry measurement, where the thickness (T) of random 15% of the droplets is measured. The electrical conductivities (σ) of all droplets are obtained using the measured and estimated film thicknesses (T). Thus, our experimental workflow can rapidly characterize the structural, optical and electrical properties of prepared samples, which are then used to create the dataset for machine learning.

2.2. Data Generation Guided by Batch Bayesian Optimization

The dataset D consists of experimental volumes of P3HT and CNT (different types) composition as well as the measured properties of the associated film. These properties include optical absorbance, absorption ratio, sheet resistance, film thickness, and film conductivity, as shown in **Table 1**. Before using the machine learning, we took logarithms of some of these values and denoted them as "R","S",'T','Y', which makes the magnitude of the noise less dependent on that of the measured values (see Figure S3, Supporting Information). To account for variance, we drop-casted six films with identical experimental inputs (C) and measured the properties of the generated films.

Table 1. Attributes of multi-labelled dataset and their corresponding symbols.

Attribute	Symbol
Composition	C
Absorbance	A
Ln(Abs. Ratio)	R
Ln(Sheet Res.)	S
Ln(Thickness)	T
Conductivity	σ
Ln(Conductivity)	Y

Next, we build our dataset through a combined batch Bayesian Optimization (BO) and regression model, as shown in **Figure 2**. BO is a heuristic global optimization algorithm that incorporates exploration in the parameter space, which could reduce the total number of experiments and account for uncertainty of the measurements. Here, we use BO, by GPyOpt package,[42] mainly for a guided exploration of parameter regions that correspond to both high and low values of R and Y, to build a dataset representative of the whole landscape.

Due to high measurement costs associated with T and Y, we only measured randomly chosen 15% of them. The rest of the properties (A, R, S) can be obtained in a high-throughput way, hence we measured all of them. We then used a regression model to populate the unmeasured values in Y, after which the BO step can continue. After every step, the regression model was updated with the newly measured values, thereby building the dataset and reducing the uncertainty. Initially, when the dataset was small, a simple linear regression model ($C \rightarrow Y$) was used to ensure good generalization. As more data was collected, we transitioned to a gradient boosting model to increase accuracy and reduce bias.

The combination of the batch BO and the regression forms our basic data generation workflow (Figure 2a). We started with a small initial dataset called 'Run 0', which was selected using a binary combination of P3HT (x%, ranging from 15% to 90%) and a single CNT type (100−x)%. From this initial set, data generation proceeded with four workflows corresponding to different targets that minimizing and maximizing R (absorbance ratio) and Y (electrical conductivity) to explore configurations of sufficiently varying conductivities and to reduce sampling bias towards high conductivity. These workflows were implemented in parallel. The collected datasets were combined at the end of the each run for subsequent machine learning tasks. The histogram and boxplot of targets during batch BO runs are given in Figure 2b, which shows the targeted exploration and the convergence of BO within very few iterations. To ensure adequate exploration of parameter space, we used a teacher-student framework: the trained machine learning model acts as an artificial representation (surrogate) of experimental ground truth. Using this surrogate model, we ran the BO in fully simulated environment over uniformly random initial samples. The results indicate that the fast convergence is due to the good initial sample spread in our experimental data and verify the adequate exploration of CNT composition space (See Section S3.4, Supporting Information for more details).
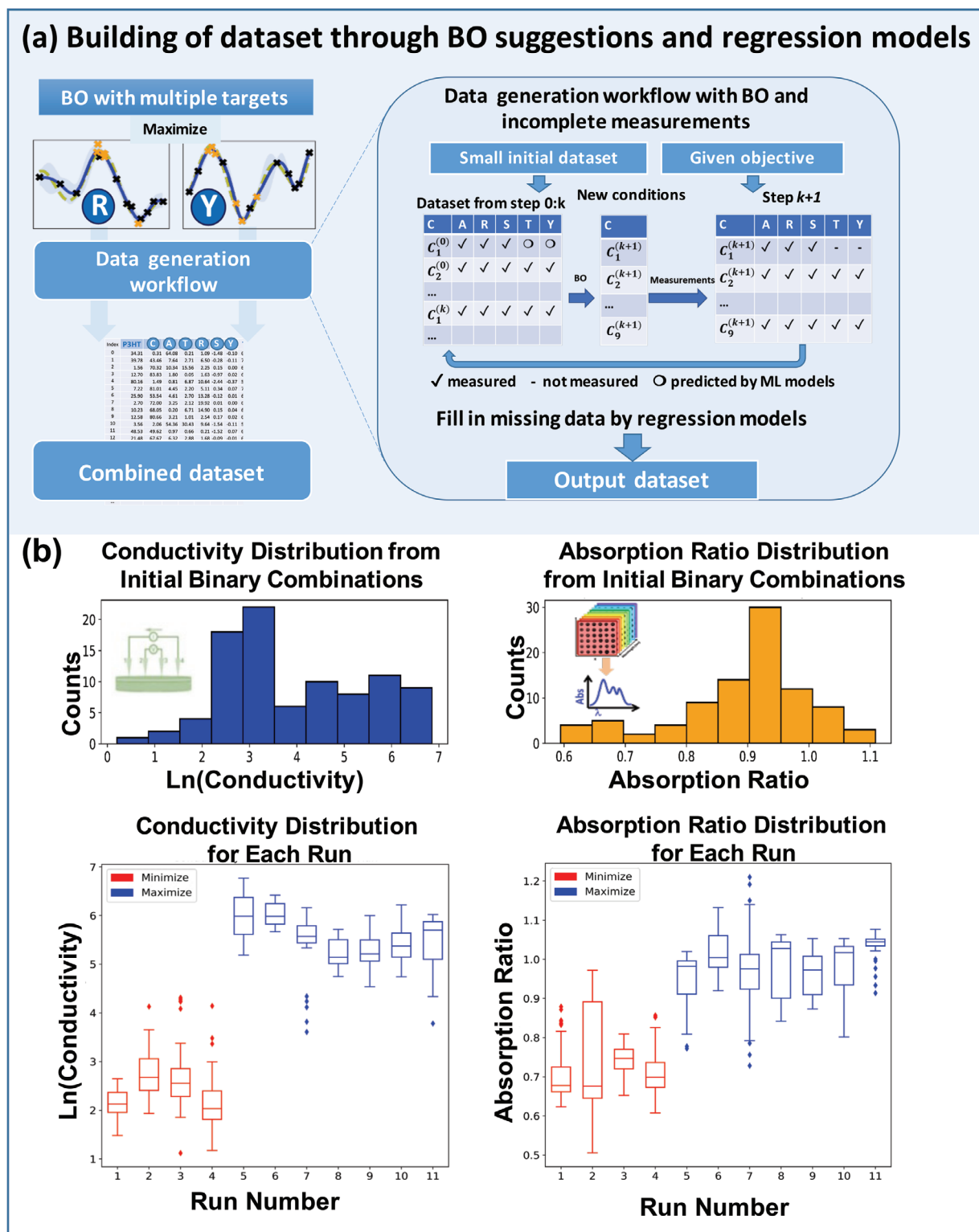
**ADVANCED
SCIENCE NEWS**
www.advancedsciencenews.com

**ADVANCED
FUNCTIONAL
MATERIALS**
www.afm-journal.de

Figure 2. Building of dataset through batch BO and regression models. The initial dataset is small and has data corresponding to composition $C_1^{(0)}, C_2^{(0)}, ...$, where $C_j^{(k)}$ refers to the jth CNT composition at the kth step of BO iteration. The dataset is updated by the "data generation workflow" in (a) with multiple targets (R and Y, minimize and maximize). For a given target, batch BO suggests new conditions $C_1^{(k+1)}, ..., C_9^{(k+1)}$, which will be added in the updated dataset after measuring the properties. Each condition has six droplets, and only 15% of all droplets have all their properties measured, while others are partially measured. The unmeasured properties are predicted by regression models (linear regression with various losses, boosting) for the next BO iteration. Finally, updated datasets corresponding to each target are combined for further machine learning tasks. The histogram and boxplot of targets during batch BO runs are given in (b).

ADVANCED
SCIENCE NEWS
www.advancedsciencenews.com

ADVANCED
FUNCTIONAL
MATERIALS
www.afm-journal.de

2.3. Graphical Regression Model for Composition-Property Relationships

In this section, we outline our design of data-driven predictive models for the relationships between composition (C) and properties. The necessity to develop novel methods comes from two challenges that commonly arise in experimental settings. First, there are multiple measurements produced, many of which are intermediate values (e.g., thickness, absorbance ratio) and are potentially incomplete. They are not the final value of interest (in contrast to conductivity), but they provide valuable information about the underlying materials system, hence the regression model should be able to fully exploit them. Second, the regression model should also capture the aspect of uncertainty due to the large experimental noise present in the measurements, which is crucial to make meaningful and reliable predictions, and to perform inverse design. We solved both of these problems by developing a graphical regression model that actively accounts for uncertainty in predictions. Such models can be used in several ways, including property prediction, inverse design, and visualization of the "landscape" of conductivity with respect to the input composition, thereby deepening our understanding of the physical system at hand. The overview of the machine learning method used in this study is shown in **Figure 3** and the detailed discussion are given in the following sections.

2.3.1. Overall Approach

In general, one can employ regression that relates only the composition (C) to conductivity σ or Y, while the graphical regression model takes multiple outputs (A, R, and S) into account to predict Y, and pursues not only the mean accuracy but also the uncertainty of the predictions due to experimental errors. Describing the composition (C) and each measured property as nodes and linking related nodes by directed edges, we can get a graph which represents the relations between composition (C) and its properties. Since our focus is on conductivity (σ or Y), we used directed acyclic graphs that have conductivity as its unique output (terminal node). Therefore, the graph G can be regarded as a structured composite function that approximates the conductivity. An example of this is $Y = F(C, R(C))$ corresponding to the graph $G_{C,1}^{(3)}$ in Figure 3, which posits that the conductivity (Y) depends directly on composition (C) and absorbance ratio (R), which is determined by composition. This introduces a sub-model $R(C)$ for the absorbance ratio-composition relationship. We trained a collection of such graphical models (with different connectivity structures), from which we selected a final model using a scoring system that accounts for both accuracy and uncertainty. We present the detailed outline of this approach in the following section.

2.3.2. Modelling and Learning Under Uncertainty

Although the film compositions are determined by user-defined experimental inputs, the nature of drop-casting introduces uncontrollable factors that affect the measured values, such as variance in film quality and, therefore, inherent characterization noise. These factors suggest that we should regard the parameters as random variables. Since the conductivity is inversely proportional to the sheet resistance and thickness ($\sigma = 1/(R_s t)$),
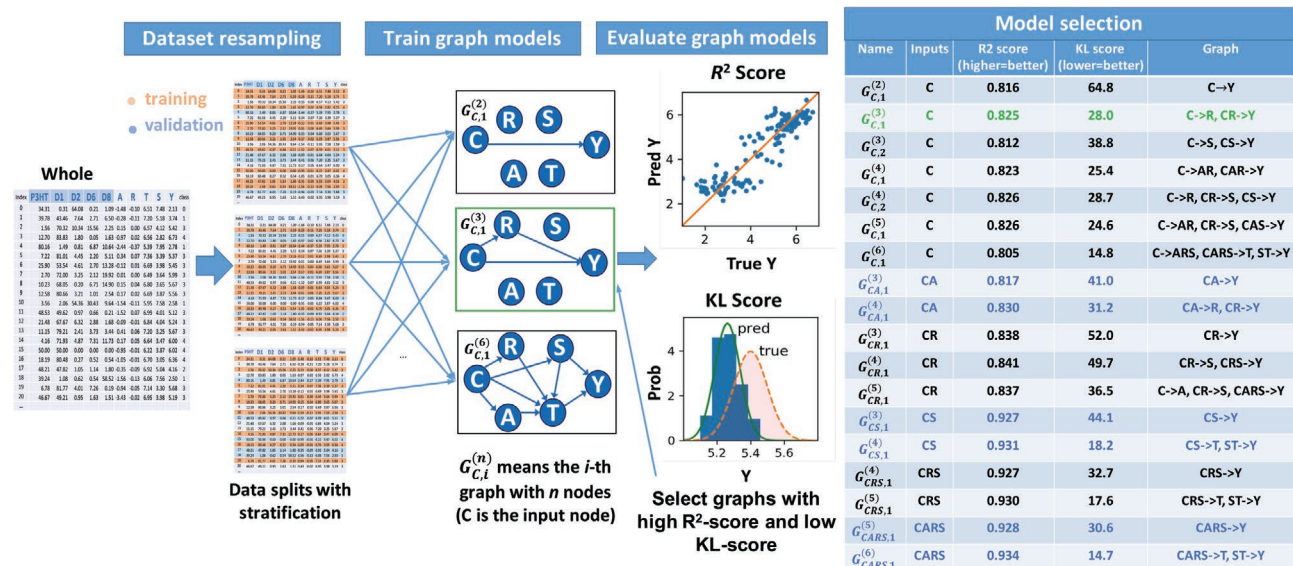

Model selection				
Name	Inputs	R2 score (higher=better)	KL score (lower=better)	Graph
$G_{C,1}^{(2)}$	C	0.816	64.8	C→Y
$G_{C,1}^{(3)}$	C	0.825	28.0	C->R, CR->Y
$G_{C,2}^{(3)}$	C	0.812	38.8	C->S, CS->Y
$G_{C,1}^{(4)}$	C	0.823	25.4	C->AR, CAR->Y
$G_{C,2}^{(4)}$	C	0.826	28.7	C->R, CR->S, CS->Y
$G_{C,1}^{(5)}$	C	0.826	24.6	C->AR, CR->S, CAS->Y
$G_{C,1}^{(6)}$	C	0.805	14.8	C->ARS, CARS->T, ST->Y
$G_{CA,1}^{(3)}$	CA	0.817	41.0	CA->Y
$G_{CA,1}^{(4)}$	CA	0.830	31.2	CA->R, CR->Y
$G_{CR,1}^{(3)}$	CR	0.838	52.0	CR->Y
$G_{CR,1}^{(4)}$	CR	0.841	49.7	CR->S, CRS->Y
$G_{CR,1}^{(5)}$	CR	0.837	36.5	C->A, CR->S, CARS->Y
$G_{CS,1}^{(3)}$	CS	0.927	44.1	CS->Y
$G_{CS,1}^{(4)}$	CS	0.931	18.2	CS->T, ST->Y
$G_{CRS,1}^{(4)}$	CRS	0.927	32.7	CRS->Y
$G_{CRS,1}^{(5)}$	CRS	0.930	17.6	CRS->T, ST->Y
$G_{CARS,1}^{(5)}$	CARS	0.928	30.6	CARS->Y
$G_{CARS,1}^{(6)}$	CARS	0.934	14.7	CARS->T, ST->Y

Figure 3. Workflow of the graphical regression method. 1) The graphical regression model is used to predict the target "Y" and its uncertainty. A graphical model, for example, $G_{C,1}^{(3)}$, is composited by some sub-regression-models, "$C{\rightarrow}R$" and "$CR{\rightarrow}Y$". The sub-models are trained 20 times by traditional method (linear regression and gradient boosting with cross-validation) using randomly chosen training datasets. During the inference phase, the sub-models (each sub-model is randomly chosen from the 20 trained ones) are composited according to the graph architecture, while the R^2-score measures the prediction accuracy. The whole dataset is randomly resampled and split into training and validation datasets, where the randomness of the training dataset is expected to capture the uncertainty of "Y", while the KL-score measures the discrepancy between prediction and true uncertainties. 2) The R^2-score and KL-score are used to select graphs which have high accuracy and low discrepancy. 3) The selected graphs are used to extract the relationship between different properties and the conductivities. 4) The scores of some selected graphs are given.

**ADVANCED
SCIENCE NEWS**
www.advancedsciencenews.com

**ADVANCED
FUNCTIONAL
MATERIALS**
www.afm-journal.de

its noise is inherited from them. Due to the fractional form, after taking a natural logarithm of these parameters, we may assume that the noise follows a normal distribution (see Section 3.1, Supporting Information for justifications for this assumption). Given the large range of conductivities that are accessible through the screening process, we model the logarithm of conductivity as,

$$Y_i \sim P_0\left(Y \mid C_i\right) = \mathcal{N}\left(\overline{Y}_i, \varepsilon_i^2\right) \tag{1}$$

where $Y_i = \log(\sigma_i)$, $\overline{Y}_i$ is the (unknown) conditional mean of Y_i given C_i and ε_i is the noise level, which is estimated to be 0.3 from data. To accommodate the uncertainties in Y, we introduced two types of randomness into the graphical regression model: random resampling of the training dataset from the original dataset $\mathcal{D}$ and random training procedure of submodels $\mathcal{M}$. Therefore, the output of a graph G describes a distribution P:

$$\hat{Y}_i \sim P\left(Y \mid C_i; G, \mathcal{D}, \mathcal{M}\right) \tag{2}$$

which is expected to approximate the distribution $P_0(Y|C_i)$. The difference between P and P_0 was minimized by model selection over various graphical models. Randomness in resampling was realized by a sub-sampling strategy that was designed to take the imbalance of $\mathcal{D}$ into account. Such imbalance arised as we used the BO to generate datasets, which caused more data to be sampled in regions with extreme objective values, since BO aims to minimize/maximize its given objective. General treatment for imbalanced datasets can be found in Torgo et al,[43] Branco et al, 2018,[44] and the details of our resampling strategy is given in Section S3.2, Supporting Information. Randomness in training procedure was realized by randomly choosing initial values and randomly searching hyper-parameters of machine learning models. The sub-models $\mathcal{M}$ in graph G were chosen from linear regression, Huber regression, and gradient-boosting models by usual cross-validation on the mean accuracy. Other models (including fully connected neural networks) were tested, but via cross-validation they were found to perform slightly worse, and hence are not included in this study. We emphasize that the randomness introduced in the dataset resampling and training procedure is not aimed to directly model the true experimental noise distribution. Rather, after introduction of some degree of noise, it becomes possible to design a strategy to select models that have the magnitude of the noise similar to the observations in the experiments. These selected models are more robust than traditional ones, which can only predict the mean of targets. The details of the model selection strategies are outlined below.

2.3.3. Graphical Regression Model Selection Strategy

With the dataset $\mathcal{D}$ and the training procedure of sub-models $\mathcal{M}$ fixed, the final model $P(Y|C_i; G, \mathcal{D}, \mathcal{M})$ depends only on graph G, and the prediction performance can be measured according to the difference between this prediction distribution $P(Y|C_i)$ and the target distribution $P_0(Y|C_i)$. A good graphical model G should have a high similarity or low distance between P and P_0. Here, we estimated this distance by two scores, namely the R^2-score and KL-score, using the mean and variance of P and P_0. The R^2-score (uses only the mean of P and P_0) is widely used as a metric for regression accuracy, and the KL-score (using both the mean and variance of P and P_0, and assuming P and P_0 are Gaussian normal distributions), named after the KL-divergence, is a measure of distance (strictly, divergence) between two probability distributions. For the graphical model selection step, we used the R^2-score as the main score (the higher the better, for mean accuracy) and KL-score (KL-divergence between $P(Y|C_i)$ and $P_0(Y|C_i)$, the lower the better, for uncertainty) as the secondary score of the graphical models. The details of the definition and typical examples of the KL-score are given in Section S3.3, Supporting Information.

3. Results

The example graphs $G_{C,i}^{(n)}$ shown in Figure 3 are those having the composition (C) as the only input, which does not require additional measurements as inputs. This special setting could provide a tool to investigate the dependence of conductivity (σ or Y) on the composition (C). Our results in Figure 3 (inset Table) show that to get predictions from C to Y, the simplest graphical model "$C \rightarrow Y$" gives a good R^2-score (0.816) but high KL-score (64.8), while the graph "$C \rightarrow R$, $CR \rightarrow Y$", could give higher R^2-score (0.825) and lower KL-score (28.0), which means the latter graphical model captures the uncertainty of Y much better. This performance improvement comes from the use of additional information from values of "A", "R", "S", and "T", rather than just the conductivity itself. Noting that addition of "A", "S", and "T" could further increase the R^2-score and decrease the KL-score, but the improvements are small, and the graphs are more complex. Therefore, we designed a weighted score that captures accuracy, uncertainty, and graph complexity simultaneously (See Section S3.1, Supporting Information for more details). The graphical model that has the highest weighted score, "$C \rightarrow R$, $CR \rightarrow Y$" was chosen as our final predictive model using C as inputs. The results shown in Figure 3 (inset Table) highlight that adding one node of "A", "R", and "S" improved the R^2-score to 0.830, 0.841, and 0.931, respectively (the KL-scores are also slightly improved). Therefore, we conclude that the most important node (disregarding thickness, since it is the most time-consuming step of the experimental workflow) to predict "Y" is the sheet-resistance (S), followed by the absorption-ratio (R), and absorbance (A), that is, "$S \gg R > A$", which is sorted by prediction improvements after the feature is taken into account. Using this order, we can further reduce experimental costs by mainly measuring the most important quantities. As a result, for this high-throughput fabrication workflow, the composition space can be effectively sampled by directly measuring the sheet resistance and final validation of the conductivity of the best performing samples can be performed by measuring the thickness of a chosen composition.

**ADVANCED
SCIENCE NEWS**
www.advancedsciencenews.com

**ADVANCED
FUNCTIONAL
MATERIALS**
www.afm-journal.de

4. High-Fidelity Experiments Based on Data Generation

We demonstrate that after 12 steps of batch BO, the maximum conductivity has no further improvement, which indicated fast convergence to locate the maximum conductivity as well as the optimal composition region. To verify this fast convergence indirectly, we designed an artificial ground truth experiment based on the graphical model, and then used the BO (same hyper-parameters with real experiments) to optimize film composition for maximum conductivity. Numerical results here indicate that seven BO steps are enough to locate the optimal region in parameter space for the artificial ground truth, with additional steps (ten more) having little improvement (for more details, refer Section S3.4, Supporting Information). Since the artificial ground truth approximates the true target as generated in our dataset, it is likely that we have found the optimal regions in our experiments as well. The feature importance analysis of both regression models (linear and gradient boosting) showed that fractions of l-SWCNT and DWCNT have the most influence on the resulting electrical performance of the final composite (see **Figure 4**a). Thus, we plot a full experimental manifold represented in a reduced 2D plot comprising only these two CNT types (Figure 4b). Interestingly, we note a local maximum in the manifold emerged at ≈10% of DWCNTs in a $L_{50}D_{10}P_{40}$ composite, which is not a common observation. In order to explore finer composition resolution, we ran additional validation experiments around this local maximum and found that the optimum is indeed reproducible, within experimental error, shown as red dot in Figure 4c.

In order to interpret the ML suggestions and understand the mechanism behind electrical conductivity of the composites, we selected four samples for comprehensive high-fidelity experimental analysis to relate the influence of P3HT/CNT composition ratio to electrical conductivity and absorption ratio. The samples included two high performing samples: $L_{60}P_{40}$ (40% P3HT and 60% long single-wall CNT), $L_{50}D_{10}P_{40}$ (40% P3HT,

10% double-wall CNT and 50% long single-wall CNT), a composite with highest performing type of CNT, but at lower concentration: $L_{10}P_{90}$ (90% P3HT and 10% long single-wall CNT), and a composite with shorter type of CNTs, but same concentration as in the highest performance one: $S_{60}P_{40}$ (40% P3HT and 60% short single-wall CNT). The electrical conductivities of the four samples were 825, 740, 200, and 15 S cm^{-1} for $L_{60}P_{40}$, $L_{50}D_{10}P_{40}$, $L_{10}P_{90}$, and $S_{60}P_{40}$ respectively. The high-fidelity measurements include absorbance spectroscopy (from UV to mid IR range) to analyze the film crystallinity and polaron delocalization, Raman spectroscopy to understand the interaction between the P3HT and CNTs, and scanning electron microscopy (SEM) to evaluate the film morphology.

In the absorbance spectra, the π-π interaction of P3HT and the polaron delocalization length, representing the film crystallinity, can be observed by monitoring the red or blue spectral shift in the visible region for undoped films and Mid-IR region for FeCl$_3$ doped film respectively (shown in **Figure 5**a,b). Pristine P3HT and FeCl$_3$ doped P3HT films were also measured for reference. All the spectra shown in Figure 5a,b are background subtracted, normalized and the Y-axis is offset in order to see the spectral features clearly. The absorption spectra of undoped $L_{60}P_{40}$, and $L_{50}D_{10}P_{40}$ in the visible region (shown in Figure 5a) clearly shows red-shifted spectral features compared to pristine P3HT, where the spectral feature due to π–π^* transition and π–π interactions of well aggregated pure polymer chains appear at around ≈2.36 and 2.06 eV respectively.[45] In addition to the red shifted spectral features, both $L_{60}P_{40}$, and $L_{50}D_{10}P_{40}$ films show fine features due to inter-band transition between van Hove singularities of single wall CNTs.[46–48] The red spectral shift due to aggregated P3HT and absorption features due to long single-wall CNTs in both $L_{60}P_{40}$, and $L_{50}D_{10}P_{40}$ films indicate 1) efficient P3HT wrapping and ordering around the well-inter connected CNT network and 2) the availability of more electronic states due to higher CNT concentration which contribute to the better electrical conductivity in these two composites compared to other films. In contrast, in the low electrical
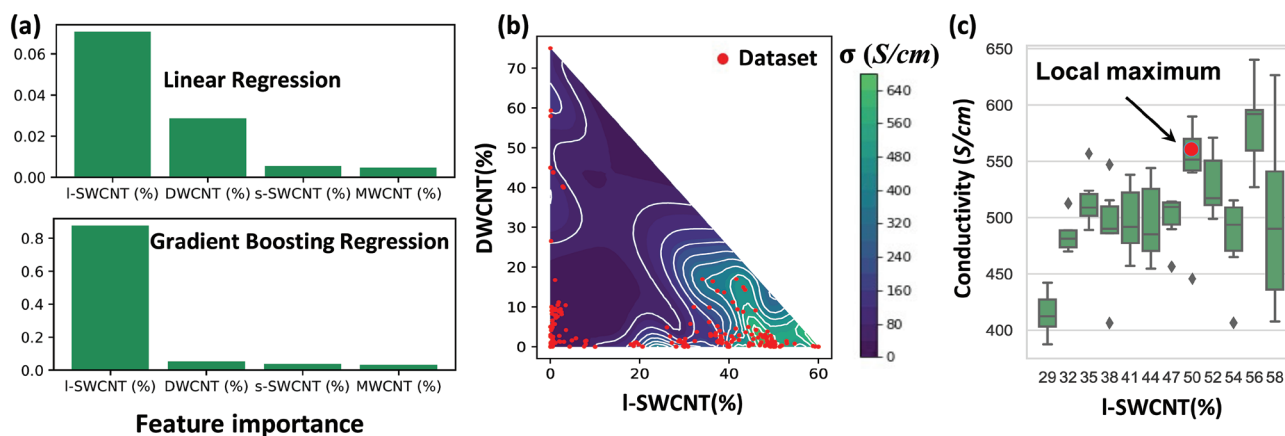

Figure 4. a) Feature importance of linear and gradient-boosting $C{\rightarrow}Y$ regression model. The top two features, l-SWCNT and DWCNT, are used to virtualize the experimental conductivity surface in (b). b) Experimental manifold with the electrical conductivity (σ) represented in the colored axis, as function of l-SWCNTs and DWCNTs compositions. Red dots are projected contents of the experiment dataset, and contour curves are provided by Gaussian-process-regression (main part of BO) with completed dataset as inputs. c) Boxplot of σ shows a local maximum at ≈10% of DWCNTs in $L_{50}D_{10}P_{40}$ composite.
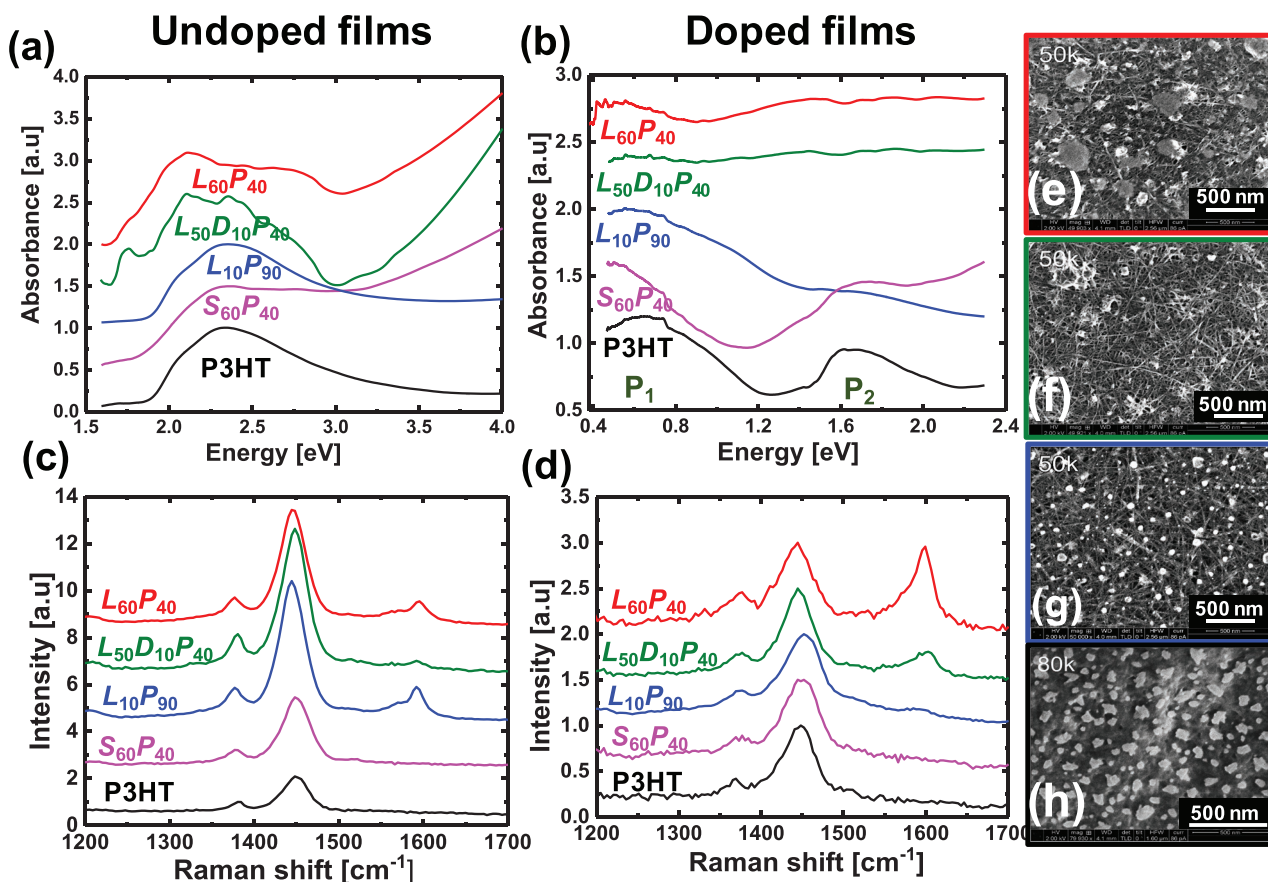
Figure 5. Optical and Morphological investigations on selected samples for interpretable ML model. a): Absorbance spectra of undoped P3HT/CNT composite films showing more red shift of absorption shoulder due to π–π interaction accompanied with fine absorption features due to CNT in both $L_{60}P_{40}$ and $L_{50}D_{10}P_{40}$ films compared to other composites; b) absorbance spectra of doped films showing the position of P1 band due to polaron delocalization; c) Raman spectra of undoped and d) doped films showing the C=C skeletal stretching vibration accompanied with "G" band vibration due to CNT and e–h) showing the SEM images of doped $L_{60}P_{40}$, $L_{50}D_{10}P_{40}$, $L_{10}P_{90}$, and P3HT films respectively.

conductivity ($S_{60}P_{40}$) sample, the spectral features due to π–π interaction are weak and shifted towards the blue region compared to P3HT, which indicates that the introduction of short single wall carbon nanotubes is not contributing to the alignment of polymer chains. The CNT fine features are also not visible in $S_{60}P_{40}$ although the percentage of CNT is 60% indicating unfavorable polymer wrapping around CNT. Both pristine P3HT and $L_{10}P_{90}$ show spectral features corresponding to well-aligned P3HT where the features due to intrachain (π–π^*) and interchain interaction (π–π) are seen clearly (Refer Figure S8, Supporting Information for the complete UV–vis–MIR spectra of all the pristine and doped films).

The absorbance spectra of FeCl$_3$ doped films are shown in Figure 5b. Doping of P3HT with FeCl$_3$ induces polaron formation that introduces two localized electronic states in the bandgap. The optical transition between these two levels create two additional absorption bands at wavelengths longer than the neutral excitons found in undoped films.[49] The high energy polaron band in FeCl$_3$ doped P3HT appears at around 1.6 eV (P2 band) and the low energy polaron band appears at around 0.5 eV (P1 band). Generally speaking, the P1 band is isolated from other optical transitions and thus it can be used to monitor the extent of polaron delocalization. Highly ordered

P3HT films doped with FeCl$_3$ have shown a distinct P1 band at 0.38 eV,[50] although the energy location and absorption strength depends on the degree of crystallinity. The absorption spectra shown in Figure 5b is normalized to the low energy peak at around 0.5 eV. The P1 peak energy measured for P3HT and $L_{10}P_{90}$ is at $\approx$0.6 eV, that shifts towards 0.5 eV in $L_{60}P_{40}$, $L_{50}D_{10}P_{40}$, and $S_{60}P_{40}$. It can be seen that the intensity of P1 band in $L_{10}P_{90}$ is much stronger and broader than the other composites indicating the wide distribution of polaron delocalization with much stronger degree of crystallinity, but its electrical conductivity is lower than $L_{60}P_{40}$ or $L_{50}D_{10}P_{40}$, indicating that the interconnectedness of the carbon nanotubes is the dominant factor contributing to the electrical conductivity of the composite films.[48]

The Raman spectra of undoped and doped films using 532 nm laser excitation are shown in Figure 5c,d. In this analysis, we focus on the prominent vibrational modes in the wavenumber region between 1300 and 1700 cm^{-1} as it explains the interaction between P3HT and CNT. The pristine P3HT shows two prominent vibrational peaks at 1382 and 1450 cm^{-1} that are assigned to C=C intra-ring and symmetric C=C stretching vibrations, consistent with literature values.[51] The Raman spectra of $L_{10}P_{90}$ shows three peaks at 1380, 1447, and

**ADVANCED
SCIENCE NEWS**
www.advancedsciencenews.com

**ADVANCED
FUNCTIONAL
MATERIALS**
www.afm-journal.de

1593 cm^{-1}, which are attributed to C–C intra-ring stretching, C=C skeletal stretching of thiophene rings and characteristic "G" band of SWNTs due to in-plane stretching of E$_{2g}$ mode.[52] The Raman spectra of L$_{60}$P$_{40}$, and L$_{50}$D$_{10}$P$_{40}$ shows the characteristic peaks of P3HT and CNT at around 1378, 1445, and 1592, however S$_{60}$P$_{40}$, which has 60% short single wall CNT does not show the characteristic "G" band signal indicating inhomogeneous distribution of carbon nanotubes. The Raman spectra of pristine CNTs are shown in Figure S9, Supporting Information.

The Raman spectra of FeCl$_3$ doped films are shown in Figure 5d. The presence of delocalized polarons shifts the symmetric C=C stretching vibrations to lower wavenumber compared to the undoped films as the presence of polarons weakens the bond strength, shifting the stretching to lower energy modes. The C=C stretching vibrations in both doped L$_{60}$P$_{40}$, and L$_{50}$D$_{10}$P$_{40}$ films exhibit larger shift towards the lower wavenumber compared to the other composites in addition to the strong "G" band contribution indicating the better degree of polaron delocalization and efficient polymer wrapping in a well-connected CNT network, which is consistent with the absorbance result shown in Figure 5b. Therefore, Absorbance and Raman spectra allow us to conclude that the better degree of polaron delocalization and well-connected CNT network with a high density of mobile charges contribute to the observed better electrical conductivity in L$_{60}$P$_{40}$, and L$_{50}$D$_{10}$P$_{40}$ films.

To further evaluate the influence of morphology on electrical conductivity, the Scanning Electron Micrographs (SEM) of doped films, L$_{60}$P$_{40}$, L$_{50}$D$_{10}$P$_{40}$, L$_{10}$P$_{90}$, and P3HT, were obtained as shown in Figure 5e–h respectively (refer Figure S10, Supporting Information for the SEM images of different magnifications). The SEM of all the three composite films (e,f) shows a homogeneous distribution of CNT wrapped with polymer; the well-interconnected CNT networks with 10% long single wall CNT concentration is shown in Figure 5f. The higher concentration of long single wall CNTs in both L$_{50}$D$_{10}$P$_{40}$ and L$_{60}$P$_{40}$ films is expected to be the differentiating factor for the higher electrical conductivity compared to the L$_{10}$P$_{90}$ film, where a higher number of mobile charges due to doped CNTs are present in the film, thereby modulating the band structure. The SEM image of $S_{60}P_{40}$ can't be obtained due to low conductivity, which is consistent with the spectroscopy features indicating that polymer wrapping in the short single wall CNTs is not favorable for electrical conduction.

5. Discussion—Beyond Validation and Broader Applications of This Methodology

We would like to emphasize the inroads we have made into application of machine learning techniques to small, but rich datasets, common in materials science. These datasets have fewer samples than typical machine learning datasets, but contain many measurements per sample, some of which are incomplete and/or are difficult to measure. In this case, the challenge for machine learning is linking the different kinds of sparse information together in order to answer a scientific hypothesis. In classical regression models, the regression function is trained from the dataset, only including the inputs and target values. In contrast, our graphical regression model takes

potentially measured proxy values, such as the absorbance ratio, into account; such practices can be generalized to other physical systems. The learned graphical models could have better prediction accuracy and uncertainty estimation. This is useful to visualize the landscape of the target, decrease measurement cost, perform inverse design, and determine relevant features for prediction (feature selection). Let us illustrate these general advantages in the specific context of our experiments.

First, we discuss how having a surrogate model can help visualize complex relationships between physical quantities. For example, during the prediction of "Y" by using the graph "C → R, CR → Y", we also predicted the value of "R". Figure 4a visualizes the landscape of "Y" and the relationship between "R" and "Y" on a subspace of compositions with only l-SWCNT and DWCNT. Using the predicted values locally, we can fit a polynomial function to smooth the landscape. For the R–Y relationship, a bilinear function could fit well, which suggests a local bilinear relationship between R and Y. This indicates that once the P3HT concentration is fixed, the ratios of carbon nanotubes determine the conductivity. This is a clear trend that is consistent with percolation theory, as the CNTs allow for delocalization of charges, and are effectively responsible for how well charges flow in the hybrid system. Therefore, for each ratio of carbon nanotubes, the P3HT plays a secondary role to hold the hybrid together, but ultimately the degree of charge transfer is controlled by the relative mixing of different CNTs.

Next, the fact that a graphical regression model can handle multiple inputs and outputs can help with data imputation (filling gaps in missing data). During data generation, we used both simple linear regression and gradient boosting models (C → Y) to predict the conductivity. However, our graphical regression model results show that we can leave some values (especially the thickness "T", whose measurement is the most time-consuming) to be unmeasured, and the learned graphical model could predict "Y" well. Therefore, the measurement costs in future experiments can be reduced. Our graphical regression model also provides a tool to determine important values to predict a given target and detect the relationships between them.

Finally, the graph-based machine learning workflow introduced in this paper forms a general approach to build models amongst multiple noisy inputs and outputs, especially when there is no a priori known relationships between them. This is a common occurrence when performing machine learning on experimental data. Our method is not only a regression model (with a fixed graph) but also a model/feature selection strategy considering both accuracy and uncertainty, with the eventual task of determining an optimal graphical model on which to build our regressor. Such an approach has resemblance to classical methods in multi-target regressions (MTR),[53–56] probabilistic graphical models (PGM),[57] and uncertainty estimation learning.[58,59] However, our problem setting is sufficiently different from usual statistical applications, and necessitates the development of novel techniques (Refer Section S3.5, Supporting Information for detailed discussion).

However, our graphical regression model-based machine learning methodology has two limitations. First, if the number

of measured attributes increases, the number of possible graph regression models increases exponentially. This makes the model selection much more expensive. Second, the current selection technique focuses on graphs with "short paths", where the output depends on input through limited number of intermediate measurements. This proved to work well for the current scientific setting, but may not be generally applicable. It is plausible that some input-output relationships may have a deep hierarchical structure. We can address both of these challenges in the future by improving on the selection techniques that minimize the number of graphs to search/optimize over, taking into account the underlying physical principles governing the system under study.

6. Conclusion

We have demonstrated a platform for machine learning-assisted high-throughput exploration and optimization for functional composites, consisting of regio-regular poly-3-hexylthiophene (P3HT), and carbon nanotubes (CNTs). The platform includes an automated flow system, drop-casting facility, hyperspectral imaging system and four-point probe for fast material processing and optical/electrical diagnostics. With the combination of this semi-automated high-throughput platform and machine learning in the loop, we showed rapid optimization of 5D composition space, achieving state-of-the-art electrical conductivity close to 1000 S cm^{-1}. Furthermore, the graphical regression model-based machine learning methodology developed here may be applied to a wide variety of problems involving noisy measurements of several values, where model selection and regression must be coupled in a principled way to achieve accurate and robust predictions.

Supporting Information

Supporting Information is available from the Wiley Online Library or from the author.

Conflict of Interest

The authors declare no conflict of interest.

Data Availability Statement

The data generated and analyzed during the current study, as well as the code implementation can be found in our repository https://github.com/Lightmann/GraphModel_for_CNTDesign.

[1] G. S. Ariggs, Mechanical pipette. **1950**, 3–5.
[2] B. P. Macleod, F. G. L. Parlane, T. D. Morrissey, F. Häse, L. M. Roch, K. E. Dettelbach, R. Moreira, L. P. E. Yunker, M. B. Rooney, J. R. Deeth, V. Lai, G. J. Ng, H. Situ, R. H. Zhang, M. S. Elliott, T. H. Haley, D. J. Dvorak, A. Aspuru-Guzik, J. E. Hein, C. P. Berlinguette, *Sci. Adv.* **2020**, *20*, eaaz8867.
[3] S. Langner, F. Häse, J. D. Perea, T. Stubhan, J. Hauch, L. M. Roch, T. Heumueller, A. Aspuru-Guzik, C. J. Brabec, *Adv. Mater.* **2020**, *32*, 1907801.
[4] B. Burger, P. M. Maffettone, V. V. Gusev, C. M. Aitchison, Y. Bai, X. Wang, X. Li, B. M. Alston, B. Li, R. Clowes, N. Rankin, B. Harris, R. S. Sprick, A. I. Cooper, *Nature* **2020**, *583*, 237.
[5] F. Ricci, W. Chen, U. Aydemir, G. J. Snyder, G.-M. Rignanese, A. Jain, G. Hautier, *Sci. Data* **2017**, *4*, 170085.
[6] A. Seko, A. Togo, H. Hayashi, K. Tsuda, L. Chaput, I. Tanaka, *Phys. Rev. Lett.* **2015**, *115*, 205901.
[7] M. W. Gaultois, T. D. Sparks, C. K. H. Borg, R. Seshadri, W. D. Bonificio, D. R. Clarke, *Chem. Mater.* **2013**, *25*, 2911.
[8] Z. M. Gibbs, F. Ricci, G. Li, H. Zhu, K. Persson, G. Ceder, G. Hautier, A. Jain, G. J. Snyder, *npj Comput. Mater.* **2017**, *3*, 8.
[9] B. Jandeleit, D. J. Schaefer, T. S. Powers, H. W. Turner, W. H. Weinberg, *Angew. Chem., Int. Ed.* **1999**, *38*, 2494.
[10] J. Wu, A. T. Bollinger, X. He, I. Božović, *Chinese Phys. B* **2018**, *27*, 118102.
[11] P. G. Schultz, X.-D. Xiang, *Curr. Opin. Solid State Mater. Sci.* **1998**, *3*, 153.
[12] A. Ludwig, *npj Comput. Mater.* **2019**, *5*, 70.
[13] N. M. Al Hasan, H. Hou, S. Sarkar, S. Thienhaus, A. Mehta, A. Ludwig, I. Takeuchi, *Engineering* **2020**, *6*, 637.
[14] B. D. Conduit, N. G. Jones, H. J. Stone, G. J. Conduit, *Mater. Des.* **2017**, *131*, 358.
[15] F. Oviedo, Z. Ren, X. Hansong, S. I. P. Tian, K. Zhang, M. Layurova, T. Heumueller, N. Li, E. Birgersson, S. Sun, B. Mayurama, I. M. Peters, C. J. Brabec, J. Fisher III, T. Buonassisi, *arXiv:2004.13599v1*, **2020**.
[16] F. Mekki-Berrada, Z. Ren, T. Huang, W. K. Wong, F. Zheng, J. Xie, I. P. S. Tian, S. Jayavelu, Z. Mahfoud, D. Bash, K. Hippalgaonkar, S. Khan, T. Buonassisi, Q. Li, X. Wang, *npj Comput. Mater.* **2020**, *7*, 55.
[17] B. D. Conduit, N. G. Jones, H. J. Stone, G. J. Conduit, *Scr. Mater.* **2018**, *146*, 82.
[18] B. D. Conduit, T. Illston, S. Baker, D. V. Duggappa, S. Harding, H. J. Stone, G. J. Conduit, *Mater. Des.* **2019**, *168*, 107644.
[19] H. Joress, B. L. DeCost, S. Sarker, T. M. Braun, S. Jilani, R. Smith, L. Ward, K. J. Laws, A. Mehta, J. R. Hattrick-Simpers, *ACS Comb. Sci.* **2020**, *22*, 330.
[20] S. Langner, F. Häse, J. D. Perea, T. Stubhan, J. Hauch, L. M. Roch, T. Heumueller, A. Aspuru-Guzik, C. J. Brabec, *Adv. Mater.* **2020**, *32*, e1907801.
[21] J. N. Kumar, Q. Li, K. Y. T. Tang, T. Buonassisi, A. L. Gonzalez-Oyarce, J. Ye, *npj Comput. Mater.* **2019**, *5*, 73.
[22] S. Nagasawa, E. Al-Naamani, A. Saeki, *J. Phys. Chem. Lett.* **2018**, *9*, 2639.
[23] Y. Wu, J. Guo, R. Sun, J. Min, *npj Comput. Mater.* **2020**, *6*, 120.

[24] F. Häse, L. M. Roch, P. Friederich, A. Aspuru-Guzik, *Nat. Commun.* **2020**, *11*, 4587.

[25] S. Wu, Y. Kondo, M.-A. Kakimoto, B. Yang, H. Yamada, I. Kuwajima, G. Lambard, K. Hongo, Y. Xu, J. Shiomi, C. Schick, J. Morikawa, R. Yoshida, *npj Comput. Mater.* **2019**, *5*, 66.

[26] P. Kumar, E. W. Zaia, E. Yildirim, D. V. M. Repaka, S.-W. Yang, J. J. Urban, K. Hippalgaonkar, *Nat. Commun.* **2018**, *9*, 5347.

[27] S. Berson, R. De Bettignies, S. Bailly, S. Guillerez, B. Jousselme, *Adv. Funct. Mater.* **2007**, *17*, 3363.

[28] M. Bernardi, M. Giulianini, J. C. Grossman, *ACS Nano* **2010**, *4*, 6599.

[29] D. H. Park, Y. K.i Hong, E. H. Cho, M.i S. Kim, D.-C. Kim, J. Bang, J. Kim, J. Joo, *ACS Nano* **2010**, *4*, 5155.

[30] M. Cai, V. T. Tiong, T. Hreid, J. Bell, H. Wang, *J. Mater. Chem. A* **2015**, *3*, 2784.

[31] C. Bounioux, P. Díaz-Chao, M. Campoy-Quiles, M. S. Martín-González, A. R. Goñi, R. Yerushalmi-Rozen, C. Müller, *Energy Environ. Sci.* **2013**, *6*, 918.

[32] Y. H. Kang, U.n-H. Lee, I.n H. Jung, S. C. Yoon, S. Y. Cho, *ACS Appl. Electron. Mater.* **2019**, *1*, 1282.

[33] S.-.H. Park, J. Hwang, G.-S.u Park, J.i-H. Ha, M. Zhang, D. Kim, D.-J. Yun, S. Lee, S. H. Lee, *Nat. Commun.* **2019**, *10*, 2537.

[34] J.-H. Li, P. Li, J.-T. Xu, C. K. Luscombe, Z.-Q. Fan, *J. Phys. Chem. C* **2016**, *120*, 27665.

[35] S. Qu, Q. Yao, L. Wang, Z. Chen, K. Xu, H. Zeng, W. Shi, T. Zhang, C. Uher, L. Chen, *NPG Asia Mater.* **2016**, *8*, e292.

[36] D. Shah, F. S. Mjalli, *Phys. Chem. Chem. Phys.* **2014**, *16*, 23900.

[37] D. T. Scholes, P. Y. Yee, J. R. Lindemuth, H. Kang, J. Onorato, R. Ghosh, C. K. Luscombe, F. C. Spano, S. H. Tolbert, B. J. Schwartz, *Adv. Funct. Mater.* **2017**, *27*, 1702654.

[38] D. T. Scholes, S. A. Hawks, P. Y. Yee, H. Wu, J. R. Lindemuth, S. H. Tolbert, B. J. Schwartz, *J. Phys. Chem. Lett.* **2015**, *6*, 4786.

[39] P. Y. Yee, D. T. Scholes, B. J. Schwartz, S. H. Tolbert, *J. Phys. Chem. Lett.* **2019**, *10*, 4929.

[40] E. Brochu, V. M. Cora, N. de Freitas, A Tutorial on Bayesian Optimization of Expensive Cost Functions, with Application to Active User Modeling and Hierarchical Reinforcement Learning. **2010**, https://www.cs.ubc.ca/tr/2009/tr-2009-23.

[41] B. Shahriari, K. Swersky, Z. Wang, R. P. Adams, N. De Freitas, *Proc. IEEE* **2016**, *104*, 148.

[42] GPyOpt: A Bayesian Optimization framework in python. http://github.com/SheffieldML/GPyOpt (accessed: August 2016).

[43] L. Torgo, R. P. Ribeiro, B. Pfahringer, P. Branco, in *SMOTE for Regression BT – Progress in Artificial Intelligence*, (Eds: L. Correia, L. P. Reis, J. Cascalho), Springer, Berlin Heidelberg **2013**, pp. 378–389.

[44] P. Branco, L. Torgo, R. P. Ribeiro, *Proceedings of Machine Learning Research* **2018**, *94*, 67.

[45] P. J. Brown, D. S. Thomas, A. Köhler, J. S. Wilson, J.i-S. Kim, C. M. Ramsdale, H. Sirringhaus, R. H. Friend, *Phys. Rev. B* **2003**, *67*, 64203.

[46] M. J. O'Connell, S. M. Bachilo, C. B. Huffman, V. C. Moore, M. S. Strano, E. H. Haroz, K. L. Rialon, P. J. Boul, W. H. Noon, C. Kittrell, J. Ma, R. H. Hauge, R. B. Weisman, R. E. Smalley, *Science (80-.).* **2002**, *297*, 593.

[47] H.-Z. Geng, D. S. Lee, K.i K. Kim, G. H. Han, H. K.i Park, Y. H. Lee, *Chem. Phys. Lett.* **2008**, *455*, 275.

[48] X. Liu, T. Pichler, M. Knupfer, J. Fink, *Phys. Rev. B* **2004**, *70*, 245435.

[49] J. Yamamoto, Y. Furukawa, *J. Phys. Chem. B* **2015**, *119*, 4788.

[50] Z. Liang, Y. Zhang, M. Souri, X. Luo, A. M. Boehm, R. Li, Y. Zhang, T. Wang, D.-Y. Kim, J. Mei, S. R. Marder, K. R. Graham, *J. Mater. Chem. A* **2018**, *6*, 16495.

[51] Y. Nakai, K. Honda, K. Yanagi, H. Kataura, T. Kato, T. Yamamoto, Y. Maniwa, *Appl. Phys. Express* **2014**, *7*, 025103.

[52] V. Saini, Z. Li, S. Bourdo, E. Dervishi, Y. Xu, X. Ma, V. P. Kunets, G. J. Salamo, T. Viswanathan, A. R. Biris, D. Saini, A. S. Biris, *J. Phys. Chem. C* **2009**, *113*, 8023.

[53] L. Breiman, J. H. Friedman, *J. R. Stat. Soc. Ser. B* **1997**, *59*, 3.

[54] E. Spyromitros-Xioufis, G. Tsoumakas, W. Groves, I. Vlahavas, *Mach. Learn.* **2016**, *104*, 55.

[55] W. Waegeman, K. Dembczyński, E. Hüllermeier, *Data Min. Knowl. Discov.* **2019**, *33*, 293.

[56] F. H. Syed, M. R. Shah, M. A. Tahir, *2020 International Conference on Emerging Trends in Smart Technologies (ICETST)*, NUCES-FAST, Karachi **2020**, pp. 1–6.

[57] D. Koller, N. Friedman, *Probabilistic Graphical Models: Principles and Techniques*, MIT Press, Cambridge, MA **2009**.

[58] Z. Ghahramani, *Nature* **2015**, *521*, 452.

[59] Y. Gal, *Uncertainty in Deep Learning*, Cambridge University **2016**.